Materials for Renewable and Sustainable Energy (2025) 14:26
https://doi.org/10.1007/s40243-025-00300-2

ORIGINAL PAPER

Stability and charge transport analysis of high-performance PM6:Y7 nonfullerene organic solar cells using the metal–insulator–metal model

Liliana Fernanda Hernández-García[1] · Luis Reséndiz[1] · Magaly Ramírez-Como[1] · Angel Sacramento[2] · Víctor Cabrera[1] · Magali Estrada[2] · Josep Pallarès[3] · Lluis F. Marsal[3]

Received: 29 February 2024 / Accepted: 19 February 2025 / Published online: 5 March 2025

Abstract
Non-fullerene acceptors are promising materials for organic solar cells because of their flexibility and low cost; however, their long-term stability remains a critical challenge. In this study, we investigate the degradation mechanisms of conventionally structured solar cells (ITO/PEDOT: PSS/PM6/Y7/PDINO/Ag) under different environmental conditions: nitrogen preservation, encapsulation, and air exposure. Using the metal-insulator-metal (MIM) model, we simulate the current-voltage characteristics and extract key parameters to understand the physical mechanisms governing device degradation. The results show that air exposure primarily affects the anode interface, reducing the interfacial dipole energy and shifting the Fermi-level alignment of PEDOT: PSS, which is crucial for efficient hole extraction. This process leads to a deterioration in the hole transport properties over time, significantly affecting device performance. In contrast, the cathodic interface remains stable, suggesting that degradation is largely driven by changes in the hole transport layer. These findings provide critical insights into the interfacial degradation mechanisms of the NFA-based solar cells. Understanding these effects will aid in the development of strategies to enhance the stability and efficiency of organic photovoltaic devices for long-term operation.

Keywords Nonfullerene organic solar cells · Anodic interface degradation · Energy alignment · Numerical simulation

Introduction

Organic solar cells (OSCs), also known as plastic solar cells, use conductive organic polymers or small organic molecules for light absorption and charge transport, thereby enabling the conversion of sunlight into electricity through the photovoltaic effect.

The developments in molecular engineering ensure the design of organic molecules optimized for optoelectronic applications. Modifying functional groups attached to the molecule or changing molecule length allows for bandgap adjustments of the material, thereby enabling optical tuning. An advantage of OSCs is their high absorption coefficient. A small amount of organic material, generally having a size in the range of hundreds of nanometers, is sufficient to absorb a large amount of light. However, OSCs present some disadvantages, including lower power conversion efficiency (PCE), stability, and strength, compared to inorganic photovoltaic cells, such as silicon solar cells. Despite these inherent challenges, the allure of OSCs lies in their lightweight construction, disposability, inexpensive fabrication, flexibility, and potential for low environmental impact. These distinctive features make polymer solar cells an attractive research topic. Recently, in the search for an ideal polymer for light absorption and charge conduction, a wide-bandgap polymer, PM6, has been developed that has

✉ Luis Reséndiz
lresendiz@ipn.mx

[1] Sección de Estudios de Posgrado e Investigación, UPIITA, Instituto Politécnico Nacional, México City 07340, México

[2] Sección de Electrónica del Estado Sólido, Departamento de Ingeniería Eléctrica, CINVESTAV–IPN, México City 07360, México

[3] Department of Electric, Electronic and Automatic Engineering, Universitat Rovira i Virgili, Tarragona 43007, Spain

shown excellent photovoltaic performance. PM6 has been successfully used to design OSC with a high PCE of > 15% [1–4], which is a crucial achievement in the field of organic photovoltaics. PM6, in conjunction with a low-band-gap nonfullerene acceptor, such as 2,2'-((2Z,2'Z)-((12,13-Bis(2-ethylhexyl)-3,9-diundecyl-12,13-dihydro- [1, 2, 5] thiadiazolo[3,4-e]thieno-[2",3'':4',5']-thieno[2',3':4,5] pyrrolo[3,2-g]thieno-[2',3':4,5]thieno[3,2-b]-indole-2,10-diyl)bis(methanylylidene))-bis(5,6-dichloro-3-oxo-2,3-dihydro-1 H-indene-2,1-diylidene))dimalononitrile (Y7), forms a bulk heterojunction with high efficiency for photon splitting and charge transfer at the interface; such an acceptor facilitates the rapid development of OSCs with the PCE exceeding 18% [5]. Additionally, OSCs utilizing PM6 in the active layer have demonstrated excellent absorption in the visible and near-infrared ranges [6], maintaining a stable morphology of the active layer over extended periods. However, nonfullerene acceptor OSCs (NFA-OSCs) present challenges that must be addressed before they can be used in commercial devices, particularly regarding their continued performance over time in the ambient atmosphere. To prevent the degradation mechanisms in the photostability of NFA-OSCs, some studies have adopted diverse strategies such as suppressing trap-mediated recombination [7] and incorporating interlayer materials or modulating the electrode work function (WF) to match the ionization potential (IP) of the donor and the electron affinity (EA) of the acceptor [8]. A well-matched WF of the anode with the IP of the donors prevents the loss of photovoltaic performance. However, an in-depth exploration of the degradation mechanisms in these devices is imperative.

Incorporating a transparent electrode into any OSC design is essential; thus, indium tin oxide (ITO) is an excellent material owing to its transparency, conductivity, and high WF. Similarly, PEDOT: PSS a commercially available and accessible polymer blend, is widely used as a buffer layer in OSCs, achieving a selective electrode for hole collection [9]. Simultaneously, it acts as an electron-blocking layer in the solar cells. Furthermore, its popularity stems from the band energy level alignment that reduces the energy barrier between ITO and the highest occupied molecular orbital (HOMO) of the active layer material [10]. To minimize the degradation effects on the OSC and enhance its efficiency, determining the energy level diagram of the materials involved in the heterostructure is crucial. Determination of the degradation effect suffered by the various layers and interfaces of an OSC and its direct consequences on the charge generation and extraction processes is possible by knowing the coupling of the energy levels of the interfaces. Herein, sophisticated experimental techniques, such as ultraviolet photoelectron spectroscopy (UPS), X-ray photoelectron spectroscopy (XPS), and cyclic voltammetry, are usually used to obtain approximated values for the IP and EA of donors and acceptors, respectively, to determine the solar cell energy configuration experimentally. However, these technologies are not feasible in all laboratories, where the performance of OSCs is studied. Thus, electrical modeling and simulation are of direct relevance in understanding the degradation effects on the electrical performance of OSC. Moreover, simulation is simpler compared to experimental techniques because simulation offers a direct and uncomplicated route to achieve the same objective. A feasible approach to determine the energy level alignment of the solar cell structure involves electrical modeling using the MIM model, which is extensively employed in electronic device physics [11]. The MIM structure comprises two metal layers that function as electrodes and are separated by an insulating layer. These components correspond to specific parts of the solar cell: Metal 1 collects the electrons generated by the solar cell; the insulator is the active material responsible for light absorption and generating electron–hole pairs; and Metal 2 collects the holes generated by the solar cell. In this study, the simulation of the current–voltage (J–V) characteristics of the cell using the MIM model is helpful to understand the consequences of the degradation of an NFA-OSC in the alignment of the energy levels between electrodes and the organic layers that constitute the structure, optimize their design, and analyze their charge extraction processes.

Herein, we analyzed the stability of NFA-OSCs by determining the WF obtained from simulating J–V characteristics under different cell degradation conditions. This study is novel compared to other studies because it helps us determine whether the degradation occurs in the active layer, i.e., at the cathode/electron-transport layer (ETL) interface or the anode/hole-transport layer (HTL) interface.

Based on the WF value in each degradation condition, we propose the alignment of the energy levels at the metal–organic interface in devices with ITO/PEDOT: PSS/PM6:Y7/PDINO/Ag structure, which provides a deeper understanding of the manner an OSC with PM6:Y7 as the active layer degrades.

Materials and methods

Cell fabrication and characterization

Conventional NFA-OSCs were fabricated using PEDOT: PSS as the HTL, PDINO as the ETL, PM6 as the donor material, and Y7 as the nonfullerene acceptor material (Fig. 1). The effective area of the device was 9 mm^2. The solar cell fabrication process was described in our previous work [1, 4].

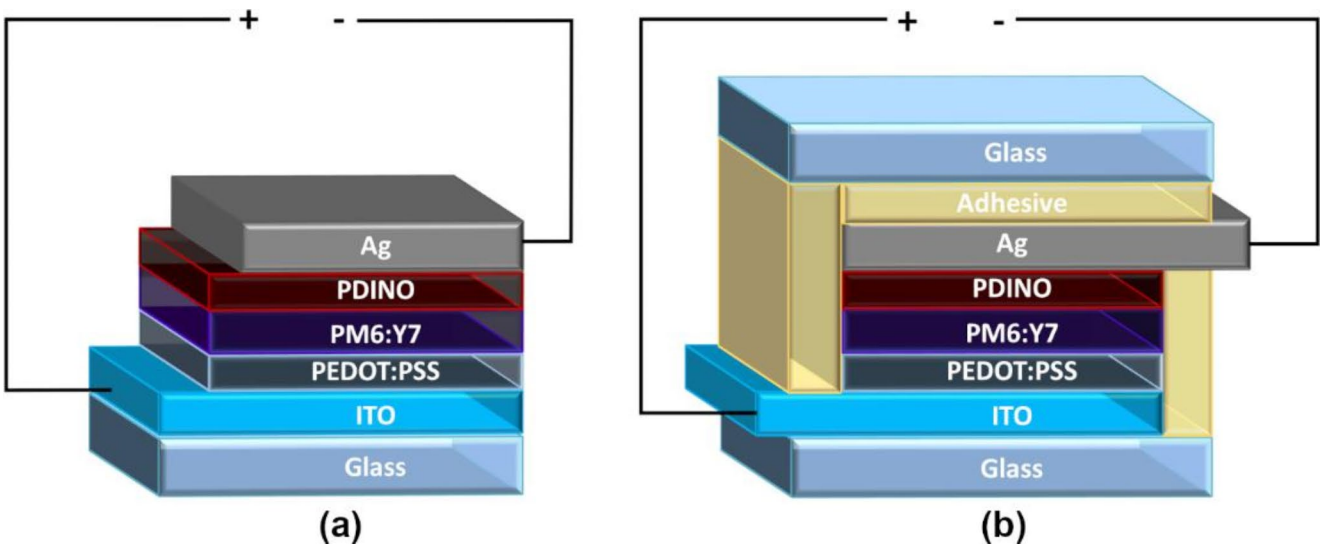

Fig. 1 Device structure of (**a**) Nonencapsulated and (**b**) Encapsulated solar cells

These solar cells were characterized under room temperature (25 °C), illuminating with a Keithley 2400 source-measure unit using a solar simulator (Abet Technologies model 11 000 class type A, Xenon arc). To prevent degradation from light exposure, the devices were only illuminated during their characterization and immediately returned to the darkness. Calibration of the solar simulator intensity yielded an AM1.5G spectrum of 100 mW/cm^2.

According to the ISOS-D-1 protocol, the solar cells were subjected to analysis under three conditions: devices maintained under a N_2 atmosphere, encapsulated devices (with the top and bottom glass sealed using NOA 68 UV light curing adhesive), and nonencapsulated devices exposed to ambient conditions (23 °C ± 2 °C and 50% ± 5% relative humidity for up to 1,000 h).

These solar cells achieved the highest initial PCE of 17.53%, corresponding to the cell preserved in the N_2 environment. The nonencapsulated cell exposed to ambient conditions immediately after fabrication exhibited a PCE of 16.46%.

Cells electrical modeling and simulation

Simulation parameters were adjusted and *J–V* characteristics were obtained by means of MIM model using numerical simulations. The simulation parameters used for the three devices included dielectric permittivity constant (ε), the effective density of states in the valence band (N_V), effective density of states in the conduction band (N_C), separation distance between electrons and holes ($a_{singlet}$) decay rate (K_{nrs}), singlet exciton binding energy ($s_{binding}$), scale factor of the photogeneration rates (b_1), and mobilities of holes (μ_h) and electrons (μ_e). The extinction coefficient and refractive index of the active layer used to simulate our work were based on the PM6:Y6 data set reported by Kerremans et al. [12]. The optical energy gap (E_g) and thickness of the active layer were obtained from experimental data by our group [1].

Despite the simplification of certain dynamic and morphological factors, the MIM model provides significant insights into the degradation mechanisms and energy-level alignment of organic solar cells. Its application aligns with previous studies that have demonstrated the efficacy of MIM-based approaches in elucidating trends in organic photovoltaic performance by focusing on bulk and interfacial charge transport phenomena [13, 14]. The MIM model is particularly well suited for identifying the dominant mechanisms affecting device performance, such as the impact of interfacial dipoles and alignment of energy levels, which are critical for understanding degradation.

However, the MIM model has inherent limitations. It does not explicitly account for complex processes, such as exciton dissociation or spatially resolved morphological effects, which are crucial for a comprehensive description of the physics of organic solar cells. Furthermore, while the MIM model simplifies charge transport as a function of interfacial conditions, more comprehensive models allow for a detailed understanding of coupled processes, including charge-carrier dynamics and excitonic behavior, across the bulk and interfaces of the device.

Nonetheless, the MIM model has proven to be computationally efficient and has demonstrated the capability to accurately reproduce the experimental *J–V* characteristics. This provides a reliable framework for analyzing trends in device degradation and identifying key interfacial processes. The insights gained from the MIM model in this

study provide a strong foundation for understanding degradation mechanisms at the interfacial level in organic solar cells.

Results and discussion

Our comprehensive analysis of nonfullerene organic solar cells (NFA-OSCs) is based on the findings of previous research [4], which demonstrates the detrimental impact of environmental humidity on the electrical performance of NFA-OSCs. In particular, the aforementioned research highlighted that humidity affects key processes within the device, such as absorption, charge separation, transport, and extraction. Moreover, the performance degradation in similar devices adheres to an exponential decay law, characterized by the superposition of two exponential functions with distinct time constants. To expand these insights, our current study delves deeper into the mechanisms behind this solar cell degradation. We measured *J–V* characteristics on nonencapsulated solar cells with ITO/PEDOT: PSS/PM6:Y7/PDINO/Ag structure to examine how these processes are impeded under humid conditions and quantify their impact on the overall device performance. Our findings demonstrate a dual-exponential decay model, which we have discussed and depicted in Fig. 2 (triangles). This model reveals the nuanced patterns of decay and offers a more refined understanding of the underlying phenomena.

Particularly, our research also contrasts the behavior of devices preserved in a nitrogen (N_2) atmosphere and encapsulated (as represented by squares and circles, respectively) in Fig. 2 with those that are not encapsulated. The former exhibits a stable open-circuit voltage (V_{OC}), while the latter shows a marked decline in this crucial parameter over time. Similarly, the N_2-preserved cell exhibited higher short-circuit current (J_{SC}) and fill factor (*FF*) compared with the cells exposed to ambient conditions. This stark difference underscores the importance of protecting NFA-OSCs from humidity to maintain performance and longevity. Our study offers a deeper understanding of the impact of environmental factors on NFA-OSCs, specifically humidity, and practical insights into the storage and handling of these devices.

Previous studies have suggested that V_{OC} in nonohmic contacts is determined using the WF difference of the electrodes; in ohmic contacts, it is determined using the lowest unoccupied molecular orbital (LUMO) and HOMO levels

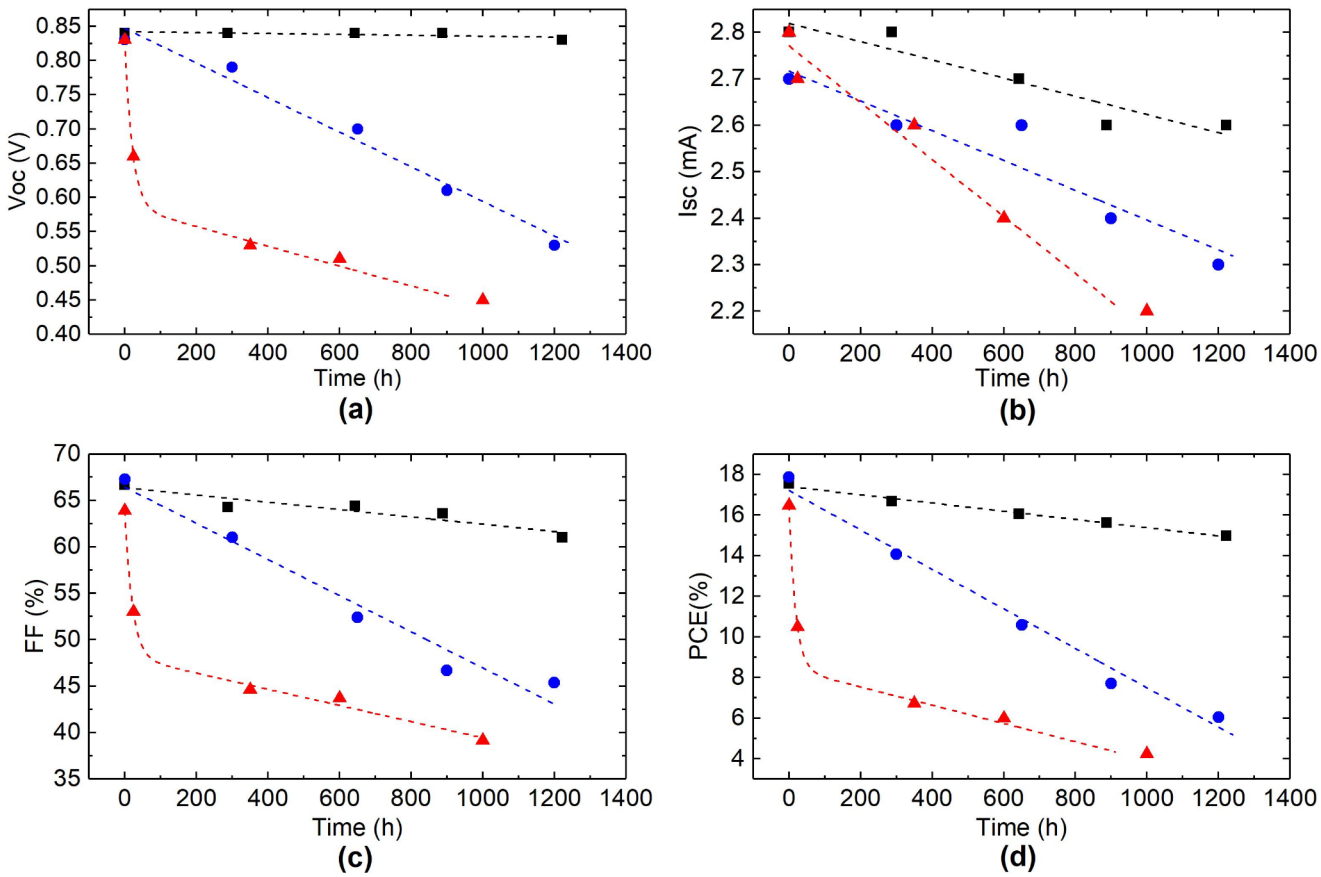

Fig. 2 Electric parameter values as a function of time of devices preserved in N_2 (squares) encapsulated devices (circles) and nonencapsulated devices (triangles). (**a**) V_{OC}, (**b**) J_{SC}, (**c**) *FF*, and (**d**) PCE of solar cells. Dashed lines serve as visual guides

of the acceptor and donor [15], respectively. However, in plastic solar cells based on fullerene derivatives, V_{OC} is directly correlated with the electron-accepting strength of fullerenes [16]. For NFA-OSCs, V_{OC} is expected to be primarily dictated by the WF of the electrodes. This crucial parameter is susceptible to alternations owing to degradation effects occurring at the metal–organic interface. Furthermore, air exposure significantly affects the stability of organic solar cells (OSCs), particularly at the anode interface in ITO/PEDOT: PSS/PM6 structures, particularly due to oxygen and moisture. The key degradation mechanisms are (1) Etching of ITO owing to the acidity of the PSS chain in the presence of air. De Jong et al. found a significant indium content in PEDOT: PSS films after casting resulting in indium diffusion into the active layer, which increased over time with both thermal annealing and exposure to air. Conversely, negligible changes in the In content in PEDOT: PSS films stored in an N_2 atmosphere at room temperature for an extended period were found. Upon removal from an N2 environment and exposure to air, considerable accelerated ITO erosion occurred [17]. Oxygen and moisture penetration lead to metal oxidation (e.g., indium or silver diffusion from ITO and Ag electrodes), increasing the resistance and causing morphological instability [18]. Therefore, we infer that in an N_2-preserved device, the minimal redistribution of In atoms at the metal–organic interface did not affect *VOC* stability, as there was no substantial degradation effect, allowing for the energy alignment of the structure to remain unchanged. (2) Exposure of the PEDOT: PSS layer to moisture present in atmospheric conditions results in an increase in the resistivity of the PEDOT: PSS/blend layer interface. This degradation of PEDOT: PSS layer appears to be spatially inhomogeneous, associated with the formation of insulating patches resulting in loss of device current and therefore device efficiency [19, 20]. (3) Susceptibility of polymers to photo-oxidation in the presence of oxygen and moisture can lead to the formation of free radicals, resulting in the breakdown of polymer chains and the creation of carbonyl and hydroxyl groups. Although not specific to PM6, the principles outlined are applicable to understanding the degradation pathway [21]. (4) The ITO layer oxidizes as a result of oxygen diffusion through the HTL, creating trap states that lower the charge mobility and increase recombination losses. The evidence that oxygen-induced interfacial oxidation modifies the charge extraction efficiency was confirmed by XPS and TOF-SIMS in a recent study on non-fullerene acceptor-based OSCs (PM6:Y7). According to Raman spectroscopy, the bulk of the active layer remained stable, but degradation was accelerated by interfacial defects [22].

To understand the evolution of layer morphology and interface changes during the degradation process in terms of device performance, we conducted numerical simulations on fabricated devices. As in previous reports, employing the MIM model allowed us to fit the experimental and simulated *J–V* characteristics [23, 24]. This alignment facilitated the identification of changes in the energy levels of the structure and their correlation with degradation processes at the anode/HTL interface of the device.

Electrical simulations of N2-preserved solar cell

Owing to the inherent complexity of directly determining the material parameters of the PM6:Y7 heterojunction, we selected the following values based on literature reports for similar organic photovoltaic materials: dielectric constant, ε, of 3.40 F/m [25], electron mobility, μ_e, of 2.98×10^{-4} cm²/Vs, and hole mobility, μ_h, of 9.67×10^{-4} cm²/Vs. The chosen values are consistent with those reported for polymer-NFA systems [26–28], ensuring their physical validity. In particular, the estimated mobility values (~10^{-4} cm²/Vs) align with the typical range observed for organic semiconductors used in organic solar cells. Although variations in these parameters can influence the device performance, previous studies have indicated that the general trends in charge transport and interfacial effects predicted by the MIM model remain valid within a reasonable range of parameter variations. Figure 3 shows the results of the simulated versus measured *J–V* characteristics of the N_2-preserved device over time. The term "fresh" device was characterized immediately after fabrication, and the remaining curves were measured at intervals after fabrication. The curves practically overlapped, indicating minimal degradation effects of the solar cell over time. Constant parameter values used for reproducing all the *J–V* characteristics during the simulation include energy band gap, $E_{g,}$of 1.33 eV [2], dielectric constant, ε, effective density of states for electrons, N_C, of 1×10^{19} cm^{-3}, effective density of sates for holes N_V of 1×10^{19} cm^{-3}, decay constant K_{nrs} of 1.82×10^6, pair electron–hole distance $a_{singlet}$ of 1.32 nm, and exciton binding energy $s_{binding}$ of 0.27 eV [23]. The constant K_{nrs} and effective density of the electron and hole states (*Nc*, *Nv*) were selected based on the results of comparable simulations of bulk heterojunction organic solar cells [29, 30]. The reported distance for the singlet exciton ($a_{singlet}$) in the charge-transfer (CT) states of non-fullerene acceptors is within the nanometer range, which is consistent with values typically used in similar modeling approaches [31]. Regarding the electrode work functions, the values determined within the MIM model represent the quantified "global effect" of energy level coupling at the interfaces. However, Riley et al. [25] reported similar work-function values in a device architecture comparable to that described in this study, further supporting the validity of the chosen parameters. Variable parameters considered

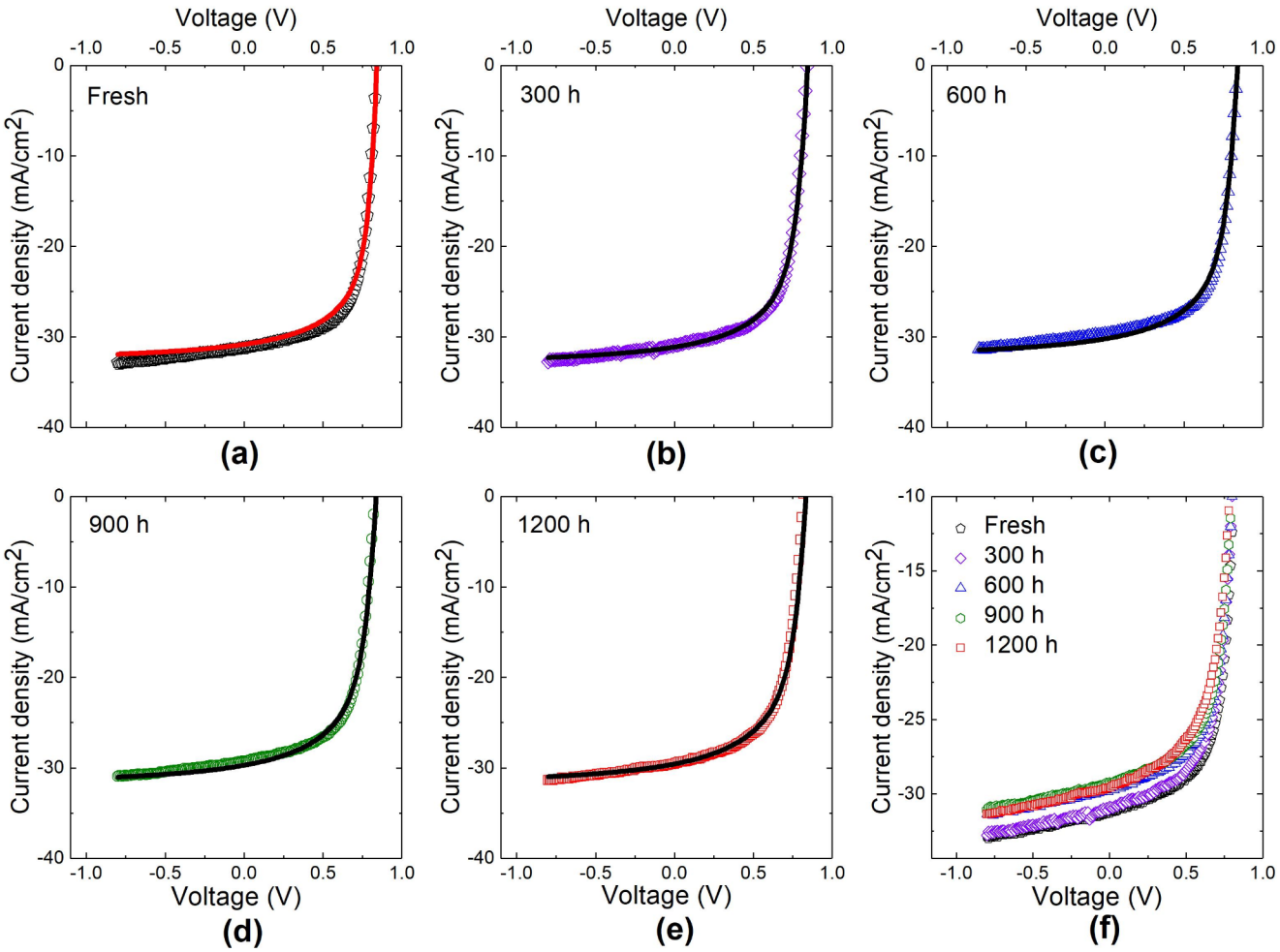

Fig. 3 *J–V* characteristics of the N_2-preserved device. Symbols denote measured curves, while solid lines represent simulated curves. (**a**) Fresh device and (**b**) 300 h, (**c**) 600 h, (**d**) 900 h, (**e**) 1,200 h after fabrication. (**f**) Device degradation effects on the *J–V* characteristics of the cell at different times

Table 1 Parameter values used in the simulation employing the metal–insulator–metal model to reproduce the *J–V* characteristics of the N_2-preserved device

Parameter	Fresh	300 (h)	650 (h)	900 (h)	1,200 (h)
b_1	0.16	0.160	0.156	0.154	0.154
WF_{Ag} (eV)	3.880	3.880	3.880	3.880	3.880
WF_{ITO} (eV)	5.150	5.150	5.150	5.150	5.150
μ_e (cm²/Vs)	2.98×10^{-4}	2.08×10^{-4}	2.08×10^{-4}	2.08×10^{-4}	2.08×10^{-4}
μ_h(cm²/Vs)	9.67×10^{-4}	7.90×10^{-4}	6.20×10^{-4}	4.90×10^{-4}	3.90×10^{-4}

for the simulation encompass photogeneration rate, b_1, Ag work function, WF_{Ag}, ITO work function, WF_{ITO}, and electron mobility, μ_e, and hole mobility, μ_h. These values for simulating the N_2-preserved devices are listed in Table 1.

Notably, μ_e remained almost constant, whereas μ_h slightly reduced. This behavior suggests that the ITO/PEDOT:PSS interface is more sensitive to changes in the chemical composition of its components than the PEDOT/Ag interface, even in an N_2 atmosphere. Moreover, reduced hole mobilities are related to hindered hole transfer from Y6 to PM6 caused by morphological defects in the active layer, as reported by Wu et al. [32]. Note that the values of the variable fitting parameters were not chosen arbitrarily. Although the choice was based on the best fit to the *J–V* experimental curve, we also considered values consistent with those obtained experimentally. In the case of electron and hole mobilities, values in the order of 10^{-4} cm/Vs were reported by our research group, which were obtained experimentally using the same device architecture [1]. In these devices, which were thermally treated to avoid intrinsic sources of traps, the trap state density is negligible, as shown through the space-charge-limited current technique for mobility measurements, as reported in previous work [1, 2]. The charge carrier mobility values of the fabricated

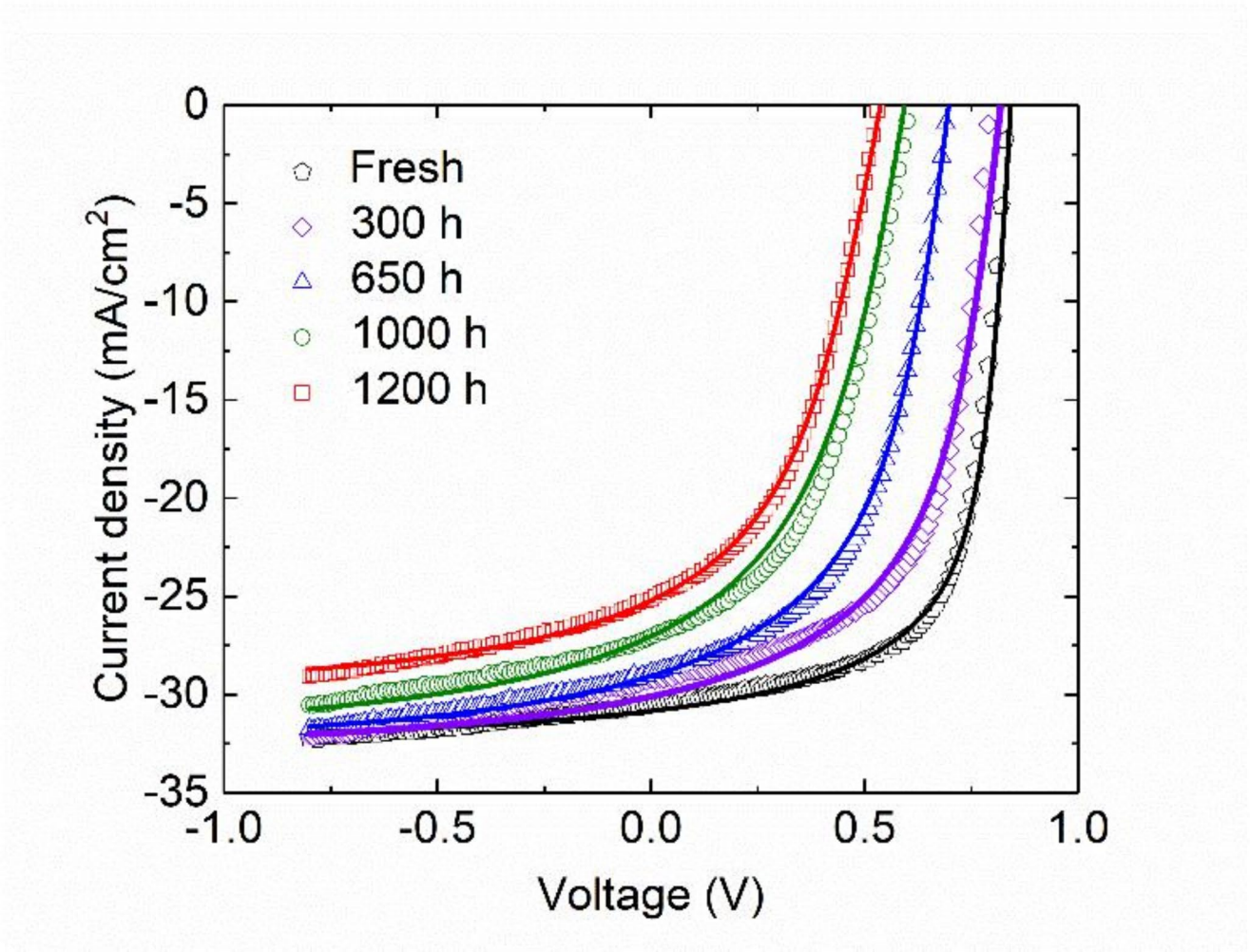

Fig. 4 *J–V* characteristics of the encapsulated device immediately after fabrication (fresh) and at 300, 650, 900, and 1,200 h after fabrication. Symbols represent measured curves, whereas solid lines depict simulated curves

Table 2 Parameter values used in simulation under the metal–insulator–metal model to reproduce the *J–V* characteristics of the encapsulated device

Parameter	Fresh	300 (h)	650 (h)	900 (h)	1,200 (h)
b_1	0.160	0.160	0.159	0.156	0.156
WF_{Ag} (eV)	3.880	3.880	3.880	3.880	3.880
WF_{ITO} (eV)	5.150	5.126	5.000	4.880	4.814
μ_e (cm²/Vs)	2.98×10^{-4}	1.2×10^{-4}	0.99×10^{-4}	0.48×10^{-4}	0.48×10^{-4}
μ_h (cm²/Vs)	9.67×10^{-4}	2.8×10^{-4}	2.73×10^{-4}	2.73×10^{-4}	2.32×10^{-4}

devices were calculated using the Mott–Gurney model. In this model, the current density (J_{SCLC}) is theoretically a function of the applied voltage (V) and is assumed to have uniform charge carrier mobility [33]. The space charge-limited mobility value is extracted from the log–log dependence of J_{SCLC} on V fitted to a slope of 2. However, in systems with high energetic disorder, a slope higher than 2 is observed, which suggests the existence of deep traps [34, 35]. Therefore, we can consider mobility as an average value with free and trapped carriers.

Electrical simulations of encapsulated solar cell

Figure 4 shows a comparison between the measured *J–V* characteristics and the simulated *J–V* characteristics of the encapsulated device. The variable parameter values considered in the simulations are presented in Table 2. In this device, the degradation effects were evident through the modification of its *J–V* characteristics. The effect of the degradation in the ITO/PEDOT: PSS interface is also corroborated by the observation that μ_h diminished to a greater extent than μ_e.

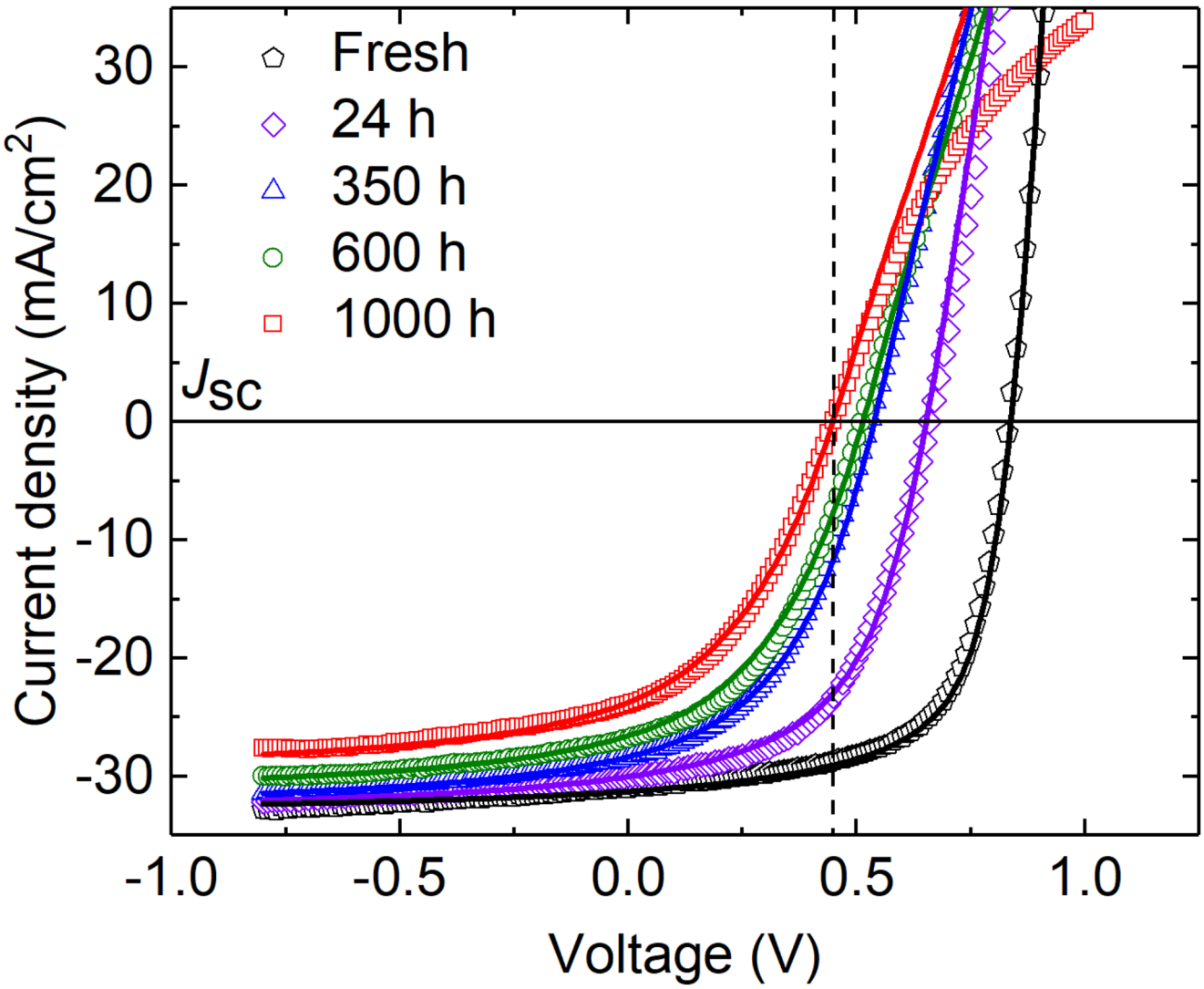

Fig. 5 *J–V* characteristics of the nonencapsulated device measured immediately after fabrication and at, 24, 350, 600, and 1,000 h after fabrication. Symbols denote measured curves, while solid lines represent simulated

Table 3 Parameter used in the simulation under the metal–insulator–metal model to reproduce the *J–V* characteristics of the nonencapsulated device

Parameter	Fresh	24 (h)	350 (h)	600 (h)	1,000 (h)
b_1	0.160	0.160	0.158	0.152	0.143
WF_{Ag} (eV)	3.880	3.880	3.880	3.880	3.880
WF_{ITO} (eV)	5.150	4.930	4.800	4.770	4.710
μ_e (cm²/Vs)	2.98×10^{-4}	8.00×10^{-5}	4.00×10^{-5}	2.80×10^{-5}	2.70×10^{-5}
μ_h (cm²/Vs)	9.67×10^{-4}	7.35×10^{-4}	6.85×10^{-4}	6.30×10^{-4}	5.00×10^{-4}

Electrical simulations of nonencapsulated solar cell

Figure 5 shows the *J–V* characteristics of the nonencapsulated device. The variable parameter values utilized in the simulations are listed in Table 3. During the most critical stage of device degradation, 1,000 h after manufacturing the device, the measured *J–V* showed an S-kink at an approximate value between 0.4 and 0.5 V. The formation of an S-shaped *J–V* characteristics at 1000 h is attributed to several factors such as the insufficient extraction of charge carriers at low internal fields, close to V_{OC} [36], imbalanced charge carrier mobility, increased series resistance within the layers, and charge accumulation at the interfaces [37].

Degradation effects at the anodic interface of OSCs exposed to the environment can increase the energy difference between the HOMO of the buffer and active layers, potentially causing charge accumulation at the interface and subsequent formation S-shaped curve formation [38].

The decrease in the built-in voltage (V_{bi}) experienced by the carriers results in an effective increase in the injection barrier at the respective electrode [39]. Herein, the V_{OC} measured 1,000 h after device fabrication exposed to the environment was 0.45 V, which is close to the voltage at which the S-kink appears. Under these device degradation conditions, as will be explained later, the calculated V_{bi} is determined to be 0.41 V, which was obtained by calculating the difference between the WF of the electrode and the energy offset resulting from the organic HOMO level owing to the formation of a dipole at the metal–organic interface.

The nonencapsulated device proves especially valuable in understanding the manifestation of degradation effects at the metal–organic interface of the device through its electronic properties. To explain this phenomenon, we proposed a simplified model to establish a connection between the charge extraction process and the degradation state of the anode–organic material interface.

As reported by Faria et al., cell degradation is evident in its *J–V* characteristics, represented by the S-kink effect due to the appearance of a potential barrier at the PEDOT: PSS/organic interface [40–42]. The vertical dashed line indicates the position of V_{bi} of the *J–V* measured after 1,000 h after device fabrication.

Fermi level and HOMO energy, denoted as E^{F}_{HOMO}, and the Fermi level and LUMO energy of the organic layer, denoted as E^{F}_{LUMO}. This case is depicted in the energy level diagram for ITO/PM6:Y7 in Fig. 6(a). The WF of ITO and Ag are 4.7 and 4.3 eV, respectively; the IP and EA of PM6:Y7 are 5.45 and 4.12 eV, respectively, as reported in a previous publication [2]. Herein, we deliberately omitted the PEDOT: PSS layer in the MIM model, considering the energy alignment of the solar cell structure as the limiting case where the effect of PEDOT: PSS completely disappears owing to interfacial degradation. Under this assumption, the E^{F}_{HOMO} of the organic layer was 0.75 eV. Nevertheless, when a metal encounters an organic material, an interfacial dipole is generated, resulting in an offset in the vacuum level. This offset is beneficial when the Fermi level of the metal matches the HOMO level of the polymer [43, 44]. Another consequence of this interfacial dipole is the increased WF of the metal (i.e., the Fermi energy decreases), leading to an increase in the HOMO energy of the organic layer by adding electrostatic energy, which further reduces the difference between the Fermi level and HOMO energy [45].

The positive impact of PEDOT: PSS on device performance as an HTL has been demonstrated [46]. We assume that this effect is due to its HOMO energy level matching with the WF of the ITO. To prove our hypothesis, we calculated the E^{F}_{HOMO} and E^{F}_{LUMO} values inferred from the effective WF of ITO and Ag, as determined from the simulation results. An energy level diagram under equilibrium conditions for the nonencapsulated "fresh" device is shown in Fig. 6(b). In this case, the WF of ITO and Ag is modified due to the formation of dipole at the interfaces because of the HTL and the ETL. The calculated interfacial dipoles for each interface are $\Delta_1 = 0.45$ eV and $\Delta_2 = 0.42$ eV, respectively.

Whitcher et al. reported a vacuum level dipole of 0.40 eV at the ITO/PEDOT: PSS interface and an effective WF of ITO as 5.05 eV measured using UPS and XPS, which are in good agreement with our calculations [47]. Yao et al. measured an effective WF of 3.88 eV for Ag employing UPS at the PDINO/Ag interface [48], corroborating the value we obtained merely through simulation. The E^{F}_{HOMO} value of 0.3 eV for the ITO/PEDOT: PSS interface and the E^{F}_{LUMO} value of 0.24 eV for the PDINO/Ag interface can be the minimum value of the interfacial energy alignment between the Fermi level of the electrode and the transport states in the organic semiconductor according to Oehzelt's theory [49]. Furthermore, Wang et al. observed that the gap states originating from organic buffer layer/fullerene layer interfaces can facilitate electron transfer in OSCs, thereby improving their efficiency and reducing the WF of the electrode [50]. During an intermediate stage of ITO/PEDOT: PSS interfacial degradation, occurring between 300 and 600 h after device fabrication, the E^{F}_{HOMO} increases, subsequently reducing the WF of the ITO. As expected, we also observed a decrease in the dipole values and the built-in voltage at ITO/PEDOT: PSS interface. The E^{F}_{LUMO} remains constant, as depicted in Fig. 6(c)–6(e). Previous reports indicate that the PDINO/Ag interface maintains ~ 90% of its initial value after 300 h of device fabrication [51], consistent with the calculations performed in this study.

In an advanced stage of device degradation, occurring 1,000 h after fabrication, PEDOT: PSS loses all its functionality as HTL at the respective electrode. The calculated interfacial dipole value for the ITO/PEDOT: PSS interface is extremely small, barely 0.01 V, as shown in Fig. 6(f). The energy diagram of the degraded device resembles the case when there is no HTL between the anode and the active layer, as shown in Fig. 6(a). As mentioned above, the calculated V_{bi} value in this condition was 0.41 V, where carrier extraction is compromised at the ITO/PEDOT: PSS interface, causing an S-kink in the *J–V* characteristics. At this degradation stage, the favorable effect of PEDOT: PSS on cell performance disappears over time. Notably, HTL and ETL were indirectly considered in the MIM model during the simulation. Thus, fitting values for the WF quantifies the "global effect" of the energy level coupling at the interfaces.

Table 4 shows the estimated values of E^{F}_{HOMO}, E^{F}_{LUMO}, and the interfacial dipole calculated from the material parameters employed in the *J–V* simulations for each device. Notably, for nonencapsulated device, as degradation advances to critical stages, the dipole value decreases and

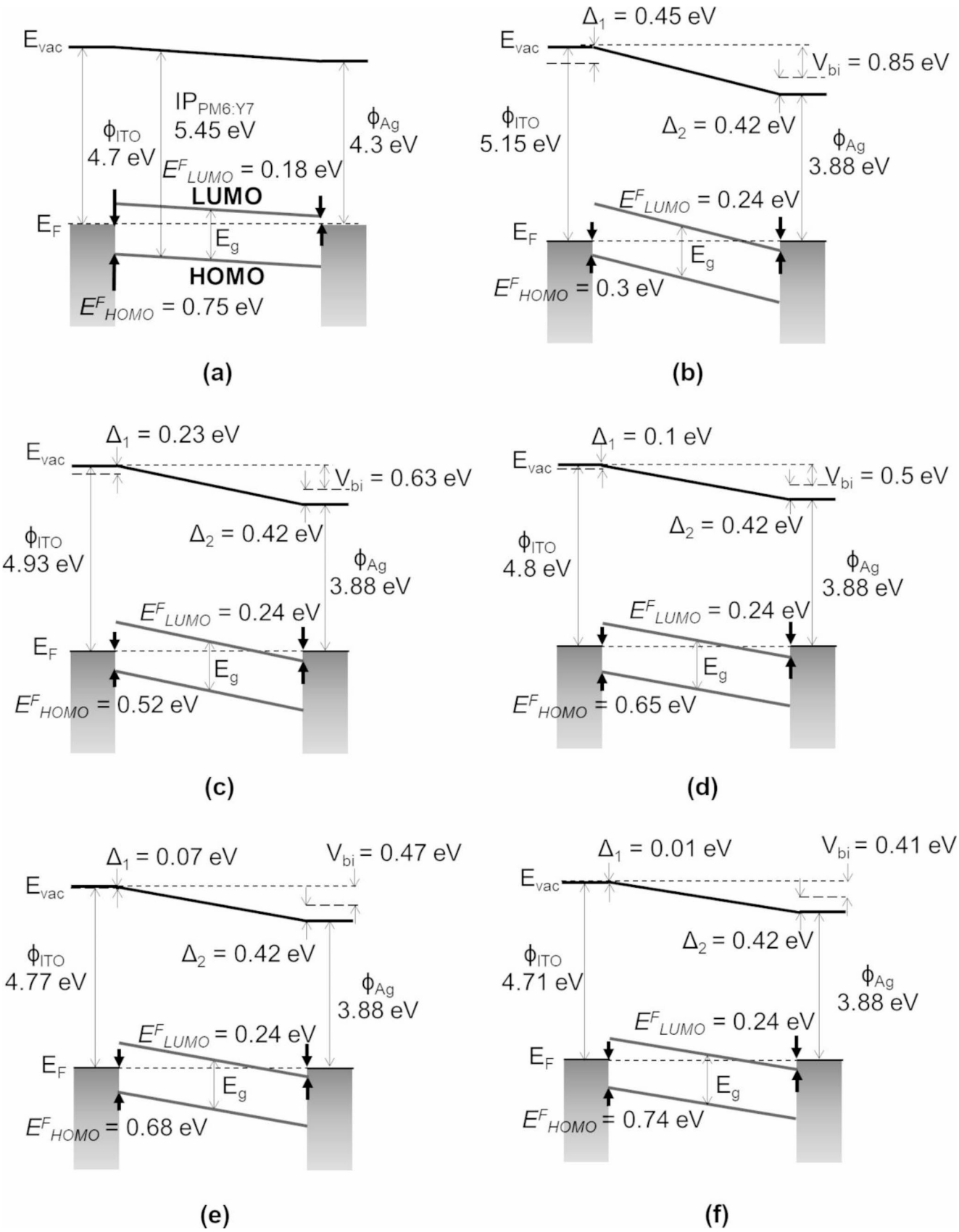

Fig. 6 Energy level alignment under the MIM model for (**a**) ITO/PM6:Y7/Ag structure, (**b**) as fabricated nonencapsulated device, (**c**) 24 h, (**d**) 350 h, (**e**) 600 h, and (**f**) 1,000 h after device fabrication

Table 4 E^{F}_{HOMO}, E^{F}_{LUMO}, and interfacial dipole offset values obtained from numerical simulations

	Time (h)	Δ_1 (eV)	Δ_2 (eV)	E^{F}_{HOMO} (eV)	E^{F}_{LUMO} (eV)
Nonencapsulated device	0	0.45	0.42	0.3	0.24
	24	0.23	0.42	0.52	0.24
	350	0.1	0.42	0.65	0.24
	600	0.07	0.42	0.68	0.24
	900	0.01	0.42	0.74	0.24
Encapsulated device	0	0.45	0.42	0.3	0.24
	300	0.43	0.42	0.31	0.24
	650	0.3	0.42	0.45	0.24
	900	0.18	0.42	0.57	0.24
	1200	0.12	0.42	0.63	0.24
N_2-preserved device	0	0.45	0.42	0.3	0.24
	300	0.45	0.42	0.3	0.24
	650	0.45	0.42	0.3	0.24
	900	0.45	0.42	0.3	0.24
	1,200	0.45	0.42	0.3	0.24

Table 5 Parameter values used in the simulation of various diodes to reproduce the *J–V* characteristics of solar cells under different environmental conditions

Encapsulated device			
Parameter	D1	D2	D3
b_1	0.160	0.168	0.180
WF_{Ag}(eV)	3.880	3.880	3.880
WF_{ITO}(eV)	5.150	5.145	5.142
μ_e(cm²/Vs)	2.98×10^{-4}	3.10×10^{-4}	3.40×10^{-4}
μ_h(cm²/Vs)	9.67×10^{-4}	1.10×10^{-3}	1.30×10^{-3}
Nonencapsulated device			
Parameter	**D1**	**D2**	**D3**
b_1	0.160	0.175	0.154
WF_{Ag}(eV)	3.880	3.880	3.880
WF_{ITO}(eV)	5.150	5.145	5.145
μ_e(cm²/Vs)	2.98×10^{-4}	2.00×10^{-4}	2.00×10^{-4}
μ_h(cm²/Vs)	9.67×10^{-4}	2.60×10^{-3}	2.89×10^{-3}
Nitrogen-preserved device			
Parameter	**D1**	**D2**	**D3**
b_1	0.160	0.172	0.180
WF_{Ag}(eV)	3.880	3.880	3.880
WF_{ITO}(eV)	5.150	5.158	5.158
μ_e(cm²/Vs)	2.98×10^{-4}	3.20×10^{-4}	3.50×10^{-4}
μ_h(cm²/Vs)	9.67×10^{-4}	1.00×10^{-3}	1.00×10^{-3}

E^{F}_{HOMO} increases for the ITO/HTL interface. Meanwhile, in all devices, the ETL/Ag interface remains stable, and the E^{F}_{LUMO} and interfacial dipole are practically constant over time.

Statistical significance test for the simulation fit parameters

To assess the statistical significance of the observed differences between the tested devices, we performed a one-factor analysis of variance (ANOVA) on the key simulation parameters: WF_{ITO}, μ_e, μ_h and parameter b_1. The *J-V* characteristics of different simulated diodes (*D1*, *D2*, and *D3*) were analyzed, and the parameter values were obtained for fresh solar cells under three conditions: encapsulated, non-encapsulated exposed to air, and nitrogen-preserved. Table 5 presents the parameter values for each condition.

A one-factor ANOVA was conducted to compare the mean values of the aforementioned parameters. The results of the data analysis are shown in Table 6. The null hypothesis is that all means are equal. Rejecting this hypothesis ensures the statistical significance of the observed differences between the mean values of the fit parameters.

The results indicate that WF_{ITO} and μ_e exhibited *p-values* below the significance level of 0.05, confirming that these parameters showed evidence of statistically significant differences among the tested conditions. This suggests that changes in the anode interface and charge transport properties due to air exposure or encapsulation have a measurable impact on device performance.

In contrast, μ_h did not show statistical significance, which is likely due to the inherent limitations of the MIM model in fully capturing the hole-transport processes across interfaces. While the model effectively representsinterfacial defects, such as recombination, trap states and resistive losses, it provides a generalized rather than a detailed description of hole mobility dynamics.

Similarly, a lack of statistical significance in parameter b_1 was expected because this parameter primarily serves as a calibration factor for aligning simulations with experimental data. Given that the photogeneration profile in the simulation cannot perfectly match the experimental conditions, small random variations in b_1 are inherent in the fitting process. However, this does not affect the overall reliability of the model, as b_1 only adjusts the short-circuit current in the simulated *J–V* characteristics without influencing other fundamental physical parameters.

These findings confirm that the estimated parameters accurately capture the primary degradation mechanisms observed under different environmental conditions, thereby reinforcing the validity of the simulation approach. The statistical significance of WF_{ITO} and μ_e highlights the sensitivity of these parameters to environmental factors, emphasizing the importance of interfacial stability for organic solar cell performance.

Conclusions

We fabricated conventional NFA-OSCs (ITO/PEDOT/PM6/PDINO/Ag) and measured their photovoltaic *J–V* characteristics over time to monitor degradation under three

Table 6 One-factor variance analysis of the simulation parameter mean values

	Origin of variations	Sum squares	Degrees of freedom	Mean squares	F – Statistic	Critical F – Value	*P* – Value
WF_{ITO}	Between groups	1.69×10^{-4}	2	8.47×10^{-5}	5.52	5.14	0.04
	Within groups	9.20×10^{-5}	6	1.53×10^{-5}			
	Total	2.61×10^{-4}	8				
μ_e	**Origin of variations**	**Sum squares**	**Degrees of freedom**	**Mean squares**	**F – Statistic**	**Critical F – Value**	**P – Value**
	Between groups	1.50×10^{-8}	2	7.54×10^{-9}	5.20	5.14	0.04
	Within groups	8.70×10^{-9}	6	1.45×10^{-9}			
	Total	2.37×10^{-8}	8				
μ_h	**Origin of variations**	**Sum squares**	**Degrees of freedom**	**Mean squares**	**F – Statistic**	**Critical F – Value**	**P – Value**
	Between groups	3.43×10^{-6}	2	1.71×10^{-6}	3.81	5.14	0.08
	Within groups	2.70×10^{-6}	6	4.50×10^{-7}			
	Total	6.13×10^{-6}	8				
b_1	**Origin of variations**	**Sum squares**	**Degrees of freedom**	**Mean squares**	**F – Statistic**	**Critical F – Value**	**P – Value**
	Between groups	1.00×10^{-4}	2	5.03×10^{-5}	0.47	5.14	0.64
	Within groups	6.39×10^{-4}	6	1.06×10^{-4}			
	Total	7.40×10^{-4}	8				

different conditions: N_2 atmosphere, encapsulation, and exposure to ambient conditions. The stability of the ITO/PEDOT interface was analyzed at different time points and correlated with the charge extraction process via numerical simulations using the MIM model. The devices preserved in the N_2 environment showed a stable anode/HTL interface, with constant interfacial dipole and E_F^{HOMO} values of 0.45 and 0.3 V, respectively, indicating that the ITO/PEDOT interface did not affect device performance. The encapsulated devices showed signs of degradation over time, such as reduced charge mobility, decreased WF_{ITO}, and degraded *J–V* characteristics. At 1,200 h after fabrication, a low interfacial dipole (0.12 V) and high E_F^{HOMO} (0.63 V) indicated energy misalignment between the WF_{ITO} and HOMO level of PEDOT, reflecting interface instability. Nonencapsulated devices showed the most advanced degradation, with the lowest PCE value of 4.5% and the appearance of an S-kink in the *J–V* characteristics, indicating a potential barrier at the ITO/PEDOT interface. The highest E_F^{HOMO} value (0.74 V) confirmed the loss of PEDOT functionality owing to the prolonged exposure to air. This study highlights the effectiveness of the proposed methodology in the qualitative and quantitative analysis of degradation effects in OSCs and predicting the consequences of electrode–organic interfacial degradation on photovoltaic performance. The agreement between experimental and simulation results enhances our understanding of the degradation mechanisms in OSCs.

Acknowledgements We would like to thank Enago (www.enago.com) for English language editing.

Author contributions Luis Reséndiz: Conceived and designed the analysis and Funding Acquisition. Liliana Fernanda Hernández-García: Performed the analysis and wrote the paper. Magaly Ramírez-Como and Angel Sacramento: Data collection. Víctor Cabrera: Review and editing. Magali Estrada, Josep Pallarès and Lluis F. Marsal: Contributed data/analysis tools.

Funding This work was supported by the Consejo Nacional de Humanidades, Ciencias y Tecnologías for the National Postdoctoral Fellowship [Curriculum Vitae number 511261, 704226 and 553956]; the Secretaría de Investigación y Posgrado del Instituto Politécnico Nacional [Project number 20232217 and 20232319].

Data availability The datasets used and/or analyzed during the current study are available from the corresponding author on reasonable request.

Declarations

Competing interests On behalf of all authors, the corresponding author states that there is no conflict of interest.

References

1. Moustafa, E., Méndez, M., Sánchez, J.G., Pallarès, J., Palomares, E., Marsal, L.F.: Thermal activation of PEDOT:PSS/PM6:Y7 based films leads to unprecedent high short-circuit current density in nonfullerene organic photovoltaics. Adv. Energy Mater. **13**, 2203241 (2023). https://doi.org/10.1002/aenm.202203241

2. Torimtubun, A.A.A., Méndez, M., Moustafa, E., Pallarès, J., Palomares, E., Marsal, L.F.: Achieving 17.7% efficiency of ternary organic solar cells by incorporating a high lowest unoccupied molecular orbital level and miscible third component. Sol RRL. **7**, 2300228 (2023). https://doi.org/10.1002/solr.202300228
3. Gokulnath, T., Gayathri, D., Park, R., Kim, H., Kim, J., Kim, H., Sudhaker Reddy, J., Yoon, S., Jin, J.: Highly efficient layer-by-layer deposition solar cells achieved with halogen-free solvents and molecular engineering of non-fullerene acceptors. Chem. Eng. J. **448**, 137621 (2022). https://doi.org/10.1016/j.cej.2022.137621
4. Ramírez-Como, M., Moustafa, E., Samir, M., Torimtubun, A.A.A., Sánchez, J.G., Pallarès, J., Marsal, L.F.: Understanding the role of interfacial layers in the photostability of PM6:Y7-based organic solar cells under different degradation conditions. Sustainable Energy Fuels. **7**, 3883–3892 (2023). https://doi.org/10.1039/D3SE00703K
5. Luo, D., Jang, W., Babu, D.D., Kim, M.S., Wang, D.H., Kyaw, A.K.K.: Recent progress in organic solar cells based on non-fullerene acceptors: Materials to devices. J. Mat. Chem. A. **10**, 3255–3295 (2022). https://doi.org/10.1039/d1ta10707k
6. Xu, T., Deng, B., Zheng, K., Li, H., Wang, Z., Zhong, Y., Zhang, C., Lévêque, G., Grandidier, B., Bachelot, R., Treguer-Delapierre, M., Qi, Y., Wang, S.: Boosting the performances of semi-transparent organic photovoltaics via synergetic Near-Infrared light management. Adv. Mater. **36**, 2311305 (2024). https://doi.org/10.1002/adma.202311305
7. Hao, X., Wang, S., Sakurai, T., Masuda, S., Akimoto, K.: Improvement of stability for small molecule organic solar cells by suppressing the trap mediated recombination. ACS Appl. Mater. Interfaces. **7**, 18379–18386 (2015). https://doi.org/10.1021/acsami.5b04334
8. Sorrentino, R., Kozma, E., Luzzati, S., Po, R.: Interlayers for non-fullerene based polymer solar cells: Distinctive features and challenges. Energy Environ. Sci. **14**, 180–223 (2021). https://doi.org/10.1039/D0EE02503H
9. Zhang, F.L., Gadisa, A., Inganäs, O., Svensson, M., Andersson, M.R.: Influence of buffer layers on the performance of polymer solar cells. Appl. Phys. Lett. **84**, 3906–3908 (2004). https://doi.org/10.1063/1.1739279
10. Jonda, C., Mayer, A.B.R., Stolz, U., Elschner, A., Karbach, A.: Surface roughness effects and their influence on the degradation of organic light emitting devices. J. Mater. Sci. **35**, 5645–5651 (2000). https://doi.org/10.1023/A:1004842004640
11. Li, D., Song, L., Chen, Y., Huang, W.: Modeling thin film solar cells: From organic to perovskite. Adv. Sci. (Weinh). **7**, 1901397 (2020). https://doi.org/10.1002/advs.201901397
12. Kerremans, R., Kaiser, C., Li, W., Zarrabi, N., Meredith, P., Armin, A.: The optical constants of solution-processed semiconductors—new challenges with perovskites and non-fullerene acceptors. Adv. Opt. Mater. **8**, 2000319 (2020). https://doi.org/10.1002/adom.202000319
13. Bartesaghi, D., Turbiez, M., Koster, L.J.A.: Charge transport and recombination in PDPP5T:[70]PCBM organic solar cells: The influence of morphology. Org. Electron. **15**, 3191–3202 (2014)
14. Mao, P., Wei, Y., Li, H., Wang, J.: Junction diodes in organic solar cells. Nano Energy. **41**, 717–730 (2017). https://doi.org/10.1016/j.nanoen.2017.10.027
15. Mihailetchi, V.D., Blom, P.W.M., Hummelen, J.C., Rispens, M.T.: Cathode dependence of the open-circuit voltage of polymer:fullerene bulk heterojunction solar cells. J. Appl. Phys. **94**, 6849–6854 (2003). https://doi.org/10.1063/1.1620683
16. Brabec, C.J., Cravino, A., Meissner, D., Sariciftci, N.S., Fromherz, T., Rispens, M.T., Sanchez, L., Hummelen, J.C.: Origin of the open circuit voltage of plastic solar cells. Adv. Funct. Mater. **11**, 374–380 (2001). https://doi.org/10.1002/1616-3028(200110)11:5<374::AID-ADFM374>3.0.CO;2-W
17. de Jong, M.P., van Ijzendoorn, L.J., de Voigt, M.J.A.: Stability of the interface between indium-tin-oxide and poly(3,4-ethylenedioxythiophene)/poly(styrenesulfonate) in polymer light-emitting diodes. Appl. Phys. Lett. **77**, 2255–2257 (2000). https://doi.org/10.1063/1.1315344
18. Dong, Q., Lei, L., Mendes, J., So, F.: Operational stability of perovskite light emitting diodes. Jrnal Phys. Mater. **3**, 012002 (2019). https://doi.org/10.1088/2515-7639/ab60c4
19. Kawano, K., Pacios, R., Poplavskyy, D., Nelson, J., Bradley, D.D.C., Durrant, J.R.: Degradation of organic solar cells due to air exposure. Sol Energy Mater. Sol Cells. **90**, 3520–3530 (2006). https://doi.org/10.1016/j.solmat.2006.06.041
20. Huang, J., Miller, P.F., Wilson, J.S., De Mello, A.J., De Mello, J.C., Bradley, D.D.C.: Investigation of the effects of doping and Post-Deposition treatments on the conductivity, morphology, and work function of Poly(3,4-ethylenedioxythiophene)/Poly(styrene sulfonate) films. Adv. Func Mater. **15**, 290–296 (2005). https://doi.org/10.1002/adfm.200400073
21. Yousif, E., Haddad, R.: Photodegradation and photostabilization of polymers, especially polystyrene: Review. SpringerPlus. **2** (2013). https://doi.org/10.1186/2193-1801-2-398
22. Flores, I., Moreno, Y.L.C., Sacramento, A., Ramírez-Como, M., Camacho, M., Cabrera, V., Rivera, C., Kudriavtsev, Y., Reséndiz, L.: Stability of Non-Fullerene Acceptor–Based organic solar cells: Chemical and physical properties at the interfaces and active layer. Mater. Res. Express. (2024). https://doi.org/10.1088/2053-1591/ad9c1a
23. Lastra, G., Balderrama, V.S., Resendiz, L., Pallarrs, J., Marsal, L.F., Cabrera, V., Estrada, M.: Air environment degradation of a high-performance inverted PTB7-Th:PC 70 BM solar cell. IEEE J. Photovolt. **9**, 464–468 (2019). https://doi.org/10.1109/JPHOTOV.2019.2892108
24. Reséndiz, L., Balderrama, V.S., Lastra, G., Ramírez, M., Cabrera, V., Estrada, M.: Optimization of PFN thickness in inverted high-performance PTB7:PC70BM solar cells. Solid State Electron. **153**, 33–36 (2019). https://doi.org/10.1016/j.sse.2018.12.013
25. Riley, D.B., Sandberg, O.J., Wilson, N.M., Li, W., Zeiske, S., Zarrabi, N., Meredith, P., Österbacka, R., Armin, A.: Direct quantification of quasi-fermi-level splitting in organic semiconductor devices. Phys. Rev. Appl. **15** (2021). https://doi.org/10.1103/PhysRevApplied.15.064035
26. Yuan, J., Zhang, Y., Zhou, L., Zhang, G., Yip, H.-L., Lau, T.-K., Lu, X., Zhu, C., Peng, H., Johnson, P.A., Leclerc, M., Cao, Y., Ulanski, J., Li, Y., Zou, Y.: Single-Junction organic solar cell with over 15% efficiency using Fused-Ring acceptor with Electron-Deficient core. Joule. **3**, 1140–1151 (2019). https://doi.org/10.1016/j.joule.2019.01.004
27. Wu, J., Sun, F., Xia, X., Franco, L.R., Chen, Q., Fu, Y., Ribeiro, R.B., Lu, X., Araujo, C.M., Wang, X., Yang, R., Guo, X., Yu, D., Zhang, M., Wang, E.: Over 18% efficiency from Halogen-Free Solvent-Processed polymer solar cells enabled by asymmetric small molecule acceptors with Fluoro-Thienyl extended terminal. Adv. Func Mater. (2025). https://doi.org/10.1002/adfm.202423137
28. Zhang, J., Han, Y., Zhang, W., Ge, J., Xie, L., Xia, Z., Song, W., Yang, D., Zhang, X., Ge, Z.: High-Efficiency thermal-Annealing-Free organic solar cells based on an asymmetric acceptor with improved thermal and air stability. ACS Appl. Mater. Interfaces. **12**, 57271–57280 (2020). https://doi.org/10.1021/acsami.0c17423
29. Lastra, G., Reséndiz, L., Ramírez-Como, M., Balderrama, V.S., Hernández-García, L.F., Marsal, L.F., Cabrera, V., Estrada, M.: Simulation of the degradation behavior of small-molecule solar cells based on p-DTS(FBTTh2)2 as the donor material. Mater.

Res. Express. **11**(065102) (2024). https://doi.org/10.1088/2053-1591/ad55b0 (b)
30. Abdelaziz, W., Shaker, A., Abouelatta, M., Zekry, A.: Possible efficiency boosting of non-fullerene acceptor solar cell using device simulation. Opt. Mat. **91**, 239–245 (2019). https://doi.org/10.1016/j.optmat.2019.03.023
31. Xie, Y., Wu, H.: Balancing charge generation and voltage loss toward efficient nonfullerene organic solar cells. Mater. Today Adv. **5**, 100048 (2020). https://doi.org/10.1016/j.mtadv.2019.100048
32. Wu, J., Lee, J., Chin, Y.-C., Yao, H., Cha, H., Luke, J., Hou, J., Kim, J.-S., Durrant, J.R.: Exceptionally low charge trapping enables highly efficient organic bulk heterojunction solar cells. Energy Environ. Sci. **13**, 2422–2430 (2020). https://doi.org/10.1039/D0EE01338B
33. Mott, N.F., Gurney, R.W.: Electronic Processes in Ionic Crystals. Oxford University Press, Oxford (1940)
34. Zuo, G., Li, Z., Andersson, O., Abdalla, H., Wang, E., Kemerink, M.: Molecular doping and trap filling in organic semiconductor host–guest systems. J. Phys. Chem. C. **121**, 7767–7775 (2017). https://doi.org/10.1021/acs.jpcc.7b01758
35. Hosseini, S.M., Tokmoldin, N., Lee, Y.W., Zou, Y., Woo, H.Y., Neher, D., Shoaee, S.: Putting order into PM6:Y6 solar cells to reduce the Langevin recombination in 400-nm Thick junction. Sol RRL. **4** (2020). https://doi.org/10.1002/solr.202000498
36. Tress, W.: Open circuit voltage and IV curve shape of ZnPc:C60 solar cells with varied mixing ratio and hole transport layer. J. Photonics Energy. **1**, 011114 (2011). https://doi.org/10.1117/1.3556726
37. Tress, W.: Organic Solar Cells. (2014). https://doi.org/10.1007/978-3-319-10097-5
38. Hao, X., Wang, S., Fu, W., Sakurai, T., Masuda, S., Akimoto, K.: Novel cathode buffer layer of Ag-doped Bathocuproine for small molecule organic solar cell with inverted structure. Org. Electron. **15**, 1773–1779 (2014). https://doi.org/10.1016/j.orgel.2014.04.030
39. Sandberg, O.J., Nyman, M., Österbacka, R.: Effect of contacts in organic bulk heterojunction solar cells. Phys. Rev. Appl. **1**, 024003 (2014). https://doi.org/10.1103/PhysRevApplied.1.024003
40. Brenes-Badilla, D., Coutinho, D.J., Amorim, D.R.B., Faria, R.M., Salvadori, M.C.: Reversing an S-kink effect caused by interface degradation in organic solar cells through gold ion implantation in the PEDOT:PSS layer. J. Appl. Phys. **123**, 155502 (2018). https://doi.org/10.1063/1.5017672
41. Araújo, F.L., Amorim, D.R.B., Coutinho, D.J., Faria, R.M.: Effects of air exposition on series and shunt resistances of a solar cell based on PTB7-Th:PC71BM. J. Mater. Sci. Mater. Electron. **30**, 16806–16811 (2019). https://doi.org/10.1007/s10854-019-01343-8
42. Gusain, A., Faria, R.M., Miranda, P.B.: Polymer solar cells-interfacial processes related to performance issues. Front. Chem. **7**, 61 (2019). https://doi.org/10.3389/fchem.2019.00061
43. Crispin, X., Geskin, V., Crispin, A., Cornil, J., Lazzaroni, R., Salaneck, W.R., Brédas, J.L.: Characterization of the interface dipole at organic/metal interfaces. J. Am. Chem. Soc. **124**, 8131–8141 (2002). https://doi.org/10.1021/ja025673r
44. Braun, S., Osikowicz, W., Wang, Y., Salaneck, W.R.: Energy level alignment regimes at hybrid organic–organic and inorganic-organic interfaces. Org. Electron. **8**, 14–20 (2007). https://doi.org/10.1016/j.orgel.2006.10.006
45. Sehati, P., Braun, S., Lindell, L., Liu, X., Andersson, L.M., Fahlman, M.: Energy-level alignment at metal-organic and organic–organic interfaces in bulk-heterojunction solar cells. IEEE J. Sel. Top. Quantum Electron. **16**, 1718–1724 (2010). https://doi.org/10.1109/JSTQE.2010.2042684
46. Maennig, B., Drechsel, J., Gebeyehu, D., Simon, P., Kozlowski, F., Werner, A., Li, F., Grundmann, S., Sonntag, S., Koch, M., Leo, K., Pfeiffer, M., Hoppe, H., Meissner, D., Sariciftci, N.S., Riedel, I., Dyakonov, V., Parisi, J.: Organic p-i-n solar cells. Appl. Phys. A. **79**, 1–14 (2004). https://doi.org/10.1007/s00339-003-2494-9
47. Whitcher, T.J., Wong, W.S., Talik, A.N., Woon, K.L., Chanlek, N., Nakajima, H., Saisopa, T., Songsiriritthigul, P.: Electrostatic model of the energy-bending within organic semiconductors: Experiment and simulation. J. Phys. Condens. Matter. **28**, 365002 (2016). https://doi.org/10.1088/0953-8984/28/36/365002
48. Yao, J., Qiu, B., Zhang, Z.G., Xue, L., Wang, R., Zhang, C., Chen, S., Zhou, Q., Sun, C., Yang, C., Xiao, M., Meng, L., Li, Y.: Cathode engineering with perylene-diimide interlayer enabling over 17% efficiency single-junction organic solar cells. Nat. Commun. **11**, 2726 (2020). https://doi.org/10.1038/s41467-020-16509-w
49. Oehzelt, M., Koch, N., Heimel, G.: Organic semiconductor density of States controls the energy level alignment at electrode interfaces. Nat. Commun. **5**, 4174 (2014). https://doi.org/10.1038/ncomms5174
50. Wang, S., Sakurai, T., Hao, X., Fu, W., Masuda, S., Akimoto, K.: Favorable electronic structure for organic solar cells induced by strong interaction at interface. J. Appl. Phys. **114** (2013). https://doi.org/10.1063/1.4829905
51. Min, J., Zhang, Z.-G., Hou, Y., Quiroz, R., Przybilla, C.O., Bronnbauer, T., Guo, C., Forberich, F., Azimi, K., Ameri, H., Spiecker, T., Li, E., Brabec, Y.: Interface engineering of perovskite hybrid solar cells with solution-processed perylene–diimide heterojunctions toward high performance. Chem. Mater. **27**, 227–234 (2015). https://doi.org/10.1021/cm5037919